

Real-space Green's function approach for intrinsic losses in x-ray spectra*

J. J. Kas and J. J. Rehr

Dept. of Physics, Univ. of Washington Seattle, WA 98195

(Dated: October 27, 2022)

Intrinsic inelastic losses in x-ray spectra originate from excitations in an interacting electron system due to a suddenly created core-hole. These losses characterize the features observed in x-ray photoemission spectra (XPS), as well as many-body effects such as satellites and edge-singularities in x-ray absorption spectra (XAS). However, they are usually neglected in practical calculations. As shown by Langreth these losses can be treated within linear response in terms of a cumulant Green's function in momentum space. Here we present a complementary *ab initio* real-space Green's function (RSGF) generalization of the Langreth cumulant in terms of the dynamically screened core-hole interaction $W_c(\omega)$ and the independent particle response function. We find that the cumulant kernel $\beta(\omega)$ is analogous to XAS, but with the transition operator replaced by the core-hole potential with monopole selection rules. The behavior reflects the analytic structure of the loss function, with peaks near the zeros of the dielectric function, consistent with delocalized quasi-boson excitations. The approach simplifies when $W_c(\omega)$ is localized and spherically symmetric. Illustrative results and comparisons are presented for the electron gas, sodium, and some early transition metal compounds.

I. INTRODUCTION

Intrinsic losses in x-ray spectra are fundamental to the photoabsorption process.¹ They originate from the dynamic response of the system to a suddenly created core-hole, leading to dynamic screening by local fields and inelastic losses. This transient response is responsible for observable effects in x-ray photoemission spectra (XPS) and x-ray absorption spectra (XAS). These include satellites due to quasi-bosonic excitations such as plasmons, charge-transfer, and shake-processes, as well as particle-hole excitations responsible for edge-singularity effects. These features are signatures of electronic correlation beyond the independent particle approximation.² Various theoretical techniques have been developed for treating these losses, including plasmon models, quasi-boson approximations, fluctuation potentials, determinantal approaches, dynamical-mean-field theories, configuration-interaction methods, and coupled-cluster approaches.^{3–15} Recently cumulant Green's function methods have been developed¹⁶ based on a real-space real-time (RSRT) generalization of the Langreth cumulant.³ While the approach gives good results for the satellites observed in XPS, even for moderately correlated systems such as transition metal oxides,^{16–18} it depends on computationally demanding real-time time-dependent density functional theory (TDDFT) calculations of the density-density response function. Thus despite these advances, quantitative calculations remain challenging, and intrinsic losses are usually neglected in current calculations of x-ray spectra.

In an effort to facilitate these calculations, we present here an *ab initio* real-space Green's function (RSGF) generalization of the Langreth cumulant complementary to the RSRT approach, in which the calculations are carried out using a discrete site-radial coordinate basis. The formalism of the cumulant kernel $\beta(\omega)$ is analogous to x-ray absorption spectra $\mu(\omega)$, except that the transition operator is replaced with the core-hole potential $V_c(\mathbf{r})$,

and the transitions are between valence and conduction states with monopole selection rules. The generalized RSGF approach thereby permits calculations of many-body effects in x-ray spectra in parallel with RSGF calculations of XAS.^{1,19} Several representations of $\beta(\omega)$ are derived, which are useful in the analysis and comparison with other approximations. For example, we show that $\beta(\omega)$ can be expressed either in terms of the bare core-hole potential $V_c(\mathbf{r})$ and the full density response function $\chi(\mathbf{r}, \mathbf{r}', \omega)$, or the dynamically screened core hole potential $W_c(\mathbf{r}, \omega)$ and the independent particle response function $\chi^0(\mathbf{r}, \mathbf{r}', \omega)$. In addition, we derive the link between the Langreth cumulant, and the commonly used approximation based on the *GW* self-energy.^{5,20,21} The potential $W_c(\mathbf{r}, \omega)$ is a key quantity of interest in this work. However, its real-space behavior does not appear to have been extensively studied heretofore. This quantity is closely related to the dynamically screened Coulomb interaction $W(\mathbf{r}, \mathbf{r}', \omega)$ used e.g., in Hedin's *GW* approximation for the one-electron self-energy.⁵ The RSGF approach simplifies when $W_c(\mathbf{r}, \omega)$ is well localized and spherically symmetric. This leads to a local model for the cumulant kernel on a 1-*d* radial grid. The local approach is tested with calculations for the homogeneous electron gas (HEG), and illustrative results are presented for nearly-free-electron systems and early 3d transition metal compounds. We find that the local model provides a good approximation for $\beta(\omega)$. The model also accounts for the Anderson edge-singularity exponent in metals. The behavior of the cumulant kernel reflects the analytic structure of the loss function, with pronounced peaks near the zeros of the dielectric function. This structure is consistent with interpretations of intrinsic excitations in terms of plasmons or charge-transfer excitations.

The remainder of this paper is organized as follows. Sec. II. summarizes the Langreth cumulant and the RSGF and RSRT generalizations. Sec. III. and IV. respectively describe the calculation details and results for the HEG and charge-transfer systems. Finally Sec. V.

contains a summary and conclusions.

II. THEORY

A. Cumulant Green's function and x-ray spectra

Intrinsic inelastic losses in x-ray spectra including particle-hole, plasmons, shake-up, etc., are characterized by features in the core-hole spectral function $A(\omega) = \sum_n |S_n|^2 \delta(\omega - \varepsilon_n)$, where S_n is the amplitude for an excitation of energy ε_n due to the creation of the core-hole. Equivalently $A_c(\omega)$ is given by the Fourier transform of the core-hole Green's function, i.e., the one-particle Green's function with a deep core-hole c created at $t = 0$ $g_c(t) = \langle 0 | c_c^\dagger e^{iHt} c_c | 0 \rangle \theta(t)$,

$$A_c(\omega) = -\frac{1}{\pi} \text{Im} \int dt e^{-i\omega t} g_c(t). \quad (1)$$

Here H is the Hamiltonian of the system while c_c^\dagger and c_c are creation and annihilation operators, respectively. The core-level XPS photocurrent $J_k(\omega) \sim A_c(\omega)$ is directly related to the spectral function, which describes both the asymmetry of the quasi-particle peak and satellites in the spectra. Intrinsic losses in x-ray absorption spectra (XAS) $\mu(\omega)$ and related spectra (e.g., EELS) from deep core-levels⁶ can be expressed in terms of a convolution of $A_c(\omega)$ and the single (or quasiparticle) XAS $\mu_1(\omega)$ ⁶

$$\mu(\omega) = \int d\omega' A_c(\omega') \mu_1(\omega - \omega'). \quad (2)$$

This accounts for effects such as satellites and the reduction factor S_0^2 in the XAS fine structure.¹ Here and below, unless otherwise noted, we use atomic units $e = \hbar = m = 1$ with distances in Bohr = 0.529 Å and energies in Hartrees = 27.2 eV. A cumulant Green's function, which is a pure exponential in the time-domain, is particularly appropriate for the treatment of intrinsic losses,

$$g_c(t) = g_c^0(t) e^{C_c(t)}, \quad (3)$$

where $g_c^0(t) = e^{i\varepsilon_c t}$ is the independent particle Green's function for a given core-level c , and $C_c(t)$ is the cumulant. This representation naturally separates single (or quasi-particle) and many-particle aspects of the final-state of the system with a deep core hole following photoabsorption, where many-body effects are embedded in the cumulant. It is convenient in the interpretation to represent the cumulant in Landau form,²²

$$C_c(t) = \int d\omega \beta(\omega) \frac{e^{i\omega t} - i\omega t - 1}{\omega^2}. \quad (4)$$

where the *cumulant kernel* $\beta(\omega)$ characterizes the strength of the excitations at a given excitation energy ω . This representation yields a normalized spectral

function, with a quasi-particle renormalization constant $Z = \exp(-a)$, where $a = \int d\omega \beta(\omega)/\omega^2$ is a dimensionless measure of correlation strength, and $\Delta = \int d\omega \beta(\omega)/\omega$ is the relaxation energy shift of the core-level.⁵⁵

B. Langreth cumulant

For a deep core-hole coupled to the interacting electron gas Langreth showed that within linear response, the intrinsic inelastic losses can be treated in terms of a cumulant Green's function, with a cumulant kernel in frequency and momentum space given by

$$\beta(\omega) = - \sum_q |V_q|^2 S(\mathbf{q}, \omega). \quad (5)$$

Here V_q is the Fourier transform of the core-hole potential and $S(\mathbf{q}, \omega)$ is the dynamic structure factor, which is directly related to time-Fourier transform of the density-density correlation function $\chi(\mathbf{q}, \omega)$ and the loss function $L(\mathbf{q}, \omega) = -\text{Im} \epsilon^{-1}(\mathbf{q}, \omega)$, i.e.,

$$\begin{aligned} S(\mathbf{q}, \omega) &\equiv -\frac{1}{\pi} \text{Im} \chi(\mathbf{q}, \omega) \theta(\omega) \\ &= -\frac{1}{\pi v_q} \text{Im} \epsilon^{-1}(\mathbf{q}, \omega) \theta(\omega), \end{aligned} \quad (6)$$

$$\chi(\mathbf{q}, \omega) = \int dt e^{i\omega t} \langle \rho_{\mathbf{q}}(t) \rho_{\mathbf{q}}(0) \rangle. \quad (7)$$

The response function $\chi(\mathbf{q}, \omega)$ can be expressed in terms of the non-interacting response $\chi^0(\mathbf{q}, \omega)$ using the relation $\chi = \chi^0 + \chi^0 K \chi$. Here the particle-hole interaction kernel K within TDDFT is given by $K = v + f_{xc}$, where $v = 4\pi/q^2$ is the bare Coulomb interaction, and $f_{xc} = \delta v_{xc}[n]/\delta n$ is the TDDFT kernel; this is obtained from the exchange-correlation potential used in the definition of the independent particle response function $\chi^0(\omega)$.

Although Langreth's expression for $\beta(\omega)$ in Eq. (5) is elegant for its simplicity, calculations of the full density response function $\chi(\mathbf{q}, \omega)$ are challenging, being comparable to that for a particle-hole Green's function or the Bethe-Salpeter equation (BSE). Moreover, the core-hole potential $V_c(\mathbf{r})$ has a long range Coulomb tail to deal with. On the other hand, the Thomas-Fermi screening length $r_0 = 0.64 r_s^{1/2}$ is short-ranged, so one may wonder to what extent a local approximation for the dynamically screened interaction might be applicable?

To this end, we note that the cumulant kernel can be expressed equivalently in terms of the dynamically screened core-hole interactions $W_{\mathbf{q}}(\omega) = V_q/\epsilon(\mathbf{q}, \omega)$ and the independent particle response function $\chi^0(\mathbf{q}, \omega)$,

$$\beta(\omega) = \frac{1}{\pi} \sum_q |V_q|^2 \text{Im} \chi(\mathbf{q}, \omega) \theta(\omega), \quad (8)$$

$$\begin{aligned} &\equiv \frac{1}{\pi} \sum_q |W_q(\omega)|^2 [\text{Im} \chi^0(\mathbf{q}, \omega) + \\ &\quad + |\chi^0(\mathbf{q}, \omega)|^2 \text{Im} f_{xc}] \theta(\omega). \end{aligned} \quad (9)$$

This equivalence is implicit in Langreth's analysis of the low energy behavior of $\beta(\omega)$ for the homogeneous electron gas (HEG) in the random phase approximation (RPA), where an adiabatic approximation is also valid $\epsilon(\mathbf{q}, \omega) \approx \epsilon(\mathbf{q}, 0)$. If the exchange correlation kernel f_{xc} is taken to be real, as in typical implementations of TDDFT or ignored as in the RPA ($f_{xc} = 0$), Eq. (10) reduces to

$$\beta(\omega) = \frac{1}{\pi} \sum_q |W_q(\omega)|^2 \text{Im} \chi^0(\mathbf{q}, \omega) \theta(\omega). \quad (10)$$

This result in terms of the screened-core-hole potential $W_q(\omega)$ can be advantageous for practical calculations in inhomogeneous systems. For example, in the adiabatic approximation $W_q(\omega) \approx W_q(0)$, only a single matrix inversion is needed to obtain $\epsilon^{-1}(\omega = 0)$, rather than an inversion at each frequency.

As a practical alternative to momentum-space, calculations of the Langreth cumulant for inhomogeneous systems have recently been carried out by transforming to real-space and real-time (RSRT).¹⁶ The approach first calculates the time-evolved density response $\delta\rho(\mathbf{r}, t)$ with the Yabana-Bertsch reformulation of TDDFT that builds in a DFT exchange-correlation kernel²³

$$\delta\rho(\mathbf{r}, t) \equiv \int d^3r' dt' \chi(\mathbf{r}, t; \mathbf{r}', t') V_c(\mathbf{r}', t'). \quad (11)$$

A Fourier transform then yields the cumulant kernel $\beta(\omega)$

$$\beta(\omega) = \text{Re} \frac{\omega}{\pi} \int_0^\infty dt e^{-i\omega t} \int d^3r V_c(\mathbf{r}) \delta\rho(\mathbf{r}, t) \theta(\omega). \quad (12)$$

This approach has been shown to give good results for a number of systems.¹⁶ However, the method requires a computationally demanding long-time evolution of the density response using a large supercell, with Kohn-Sham DFT calculations at each time-step. In addition, a post-processing convolution is needed for XAS calculations.

C. Real-space Green's function Cumulant

Our primary goal in this work is to develop an alternative, real-space Green's function formulation of the Langreth cumulant and its key ingredients. In particular we aim to investigate the behavior of the cumulant kernel $\beta(\omega)$ and the dynamically screened core-hole potential $W_c(\mathbf{r}, \omega)$. The method is complementary to the RSRT formulation but is based on a similar approach for the response function, and can be carried out in parallel with RSGF calculations of XAS.^{1,24} Within the RPA, the RSGF formulation of $\beta(\omega)$ can be derived from the perhaps better known GW approximation to the cumulant, based on the core-level self-energy $\Sigma_c(\omega)$,^{20,21,25}

$$\beta(\omega) = \frac{1}{\pi} \text{Im} \Sigma_c(\epsilon_c - \omega), \quad (13)$$

where $\Sigma_c(\omega) = \langle c | \Sigma(\omega) | c \rangle$. This matrix element can be evaluated in real-space using the GW approximation

$$\text{Im} \Sigma(\mathbf{r}, \mathbf{r}', \omega) = - \sum_i^{occ} \psi_i(\mathbf{r}) \psi_i(\mathbf{r}') \times \text{Im}[W(\mathbf{r}, \mathbf{r}', \epsilon_i - \omega)] \theta(\epsilon_i - \omega), \quad (14)$$

where $W(\mathbf{r}, \mathbf{r}', \omega)$ is the dynamically screened Coulomb interaction. Within the decoupling approximation,²¹ the core-level wave-function is assumed to have no overlap with any other electrons, and Eq. (13) becomes

$$\beta(\omega) = \frac{1}{\pi} \text{Im} \int d^3r d^3r' \rho_c(\mathbf{r}) W(\mathbf{r}, \mathbf{r}', \omega) \rho_c(\mathbf{r}') \theta(\omega) \quad (15)$$

$$= \frac{1}{\pi} \text{Im} \int d^3r \rho_c(\mathbf{r}) W_c(\mathbf{r}, \omega) \theta(\omega), \quad (16)$$

where $W_c(\mathbf{r}, \omega) = \int d^3r' W(\mathbf{r}, \mathbf{r}', \omega) \rho_c(\mathbf{r}')$ and $\rho_c(\mathbf{r}) = |\psi_c(\mathbf{r})|^2$. Then noting that $\text{Im} W_c = \text{Im} [K \chi V_c]$ (indices suppressed for simplicity) and within the RPA ($K = v$), we obtain a real-space generalization of the Langreth cumulant in Eq. (8)

$$\beta(\omega) = \frac{1}{\pi} \int d^3r d^3r' V_c(\mathbf{r}) V_c(\mathbf{r}') \text{Im} \chi(\mathbf{r}, \mathbf{r}', \omega) \theta(\omega). \quad (17)$$

This result is also equivalent to the RSRT expression in Eq. (12). Alternatively, in analogy with Eq. (10), and again within the RPA, $\beta(\omega)$ can be expressed in terms of $W_c(\mathbf{r}, \omega)$ and the independent particle response function

$$\beta(\omega) = \frac{1}{\pi} \int d^3r d^3r' W_c^*(\mathbf{r}, \omega) W_c(\mathbf{r}', \omega) \times \text{Im} \chi^0(\mathbf{r}, \mathbf{r}', \omega) \theta(\omega). \quad (18)$$

While Eqs. (16-18) are formally equivalent within the RPA, they differ if the interaction kernel K is complex (which is the case for most non-adiabatic kernels), in which case it is not obvious which approximation is best. Here we focus on the RPA expressions only, although a generalization to adiabatic f_{xc} would be relatively simple.

The static limit of Eq. (18) is interesting in itself. At frequencies well below ω_p , the core-hole potential is strongly screened beyond the screening length r_0 and nearly static. On expanding $\chi(\mathbf{r}, \mathbf{r}', \omega)$ about $\omega = 0$ and keeping only the leading terms, one obtains the adiabatic approximation

$$\beta(\omega) \approx \frac{1}{\pi} \int d^3r d^3r' W_c^*(\mathbf{r}, 0) W_c(\mathbf{r}', 0) \text{Im} \chi^0(\mathbf{r}, \mathbf{r}', \omega). \quad (19)$$

This limiting behavior is similar to the adiabatic TDDFT approximation for XAS,²⁶ but with the replacement of the dipole operator $d(\mathbf{r})$ by the statically screened core-hole potential $W_c(\mathbf{r}, 0)$. This potential is also used in calculations of XAS to approximate the particle-hole interaction, and is similar to the *final state rule* approximation for the static core-hole potential.

The transformation in Eq. (16) emphasizes the localization of $\beta(\omega)$, which only depends on the imaginary part of the screened core-hole potential $\text{Im } W_c(\mathbf{r}, \omega)$ over the range of the core density $\rho_c(\mathbf{r})$. The above identities also illustrate the connection between the local and extended behavior of the dynamical response function. This connection is analogous, e.g., to the origin of fine-structure in XAS, where back-scattering is responsible for the fine-structure in photoelectron wave-function at the origin.

Not surprisingly, since both quantities are physically related to dielectric response, calculations of $\beta(\omega)$ are formally similar to those for XAS.²⁷

$$\mu(\omega) = \frac{4\pi}{V} \int d^3r d^3r' d(\mathbf{r})d(\mathbf{r}') \text{Im } \chi(\mathbf{r}, \mathbf{r}', \omega), \quad (20)$$

where $d(\mathbf{r})$ is the (e.g., dipole) transition operator. Analogous expressions have been derived for TDDFT approximations of atomic polarizabilities^{28,29} and optical absorption spectra.²⁶ The quasi-particle XAS $\mu_1(\omega)$ in our RSGF calculations^{1,24} is obtained by evaluating $\mu(\omega)$ using the final-state rule, i.e., with a screened core-hole in the final state, which corresponds to the adiabatic approximation of Eq. (19). Physically the absorption in $\mu(\omega)$ can be viewed in terms of the damped oscillating electric dipole moment of the system induced by an external electric dipole potential oscillating at frequency ω . The kernel $\beta(\omega)$ can be viewed similarly, except that the dipole potential $d(\mathbf{r})$ is replaced by the core-hole potential $V_c(\mathbf{r})$. Thus a major difference is that the suddenly turned on core-hole induces a damped oscillating monopole response field about the absorbing atom.

Formally $W_c(\mathbf{r}, \omega)$ can be calculated in terms of the inverse TDDFT dielectric matrix in real-space²⁸

$$W_c(\mathbf{r}, \omega) = \int d^3r' \epsilon^{-1}(\mathbf{r}, \mathbf{r}', \omega) V_c(\mathbf{r}'), \quad (21)$$

$$\epsilon(\mathbf{r}, \mathbf{r}', \omega) = \delta(\mathbf{r}, \mathbf{r}') - \int d^3r'' K(\mathbf{r}, \mathbf{r}'') \chi^0(\mathbf{r}'', \mathbf{r}', \omega) \quad (22)$$

Related expressions for $W_c(\mathbf{r}, \omega)$ in atoms have also been reported.³⁰ Alternatively $W_c(\mathbf{r}, \omega)$ can be obtained by iterating the integral equation $W_c = V_c + K\chi^0 W_c$ to self-consistency.²⁸ Yet another tack is the use of *fluctuation potentials*, e.g., in the quasi-boson approach.⁵ These are obtained by diagonalizing the dielectric matrix using an eigenvalue problem for each frequency ω ,

$$\int d^3r' \epsilon(\mathbf{r}, \mathbf{r}', \omega) w_s(\mathbf{r}', \omega) = \lambda_s(\omega) w_s(\mathbf{r}, \omega), \quad (23)$$

The eigenfunctions $w_s(\omega)$ are the same as those for $K\chi^0$, which has eigenvalues $\kappa_s(\omega) = 1 - \lambda_s(\omega)$. This approach is particularly useful near the quasi-bosonic resonances $\omega_s = \omega_p$ where $\text{Re } \lambda_p(\omega)$ crosses zero and matrix inversion can be numerically unstable. The corresponding excitation energies ω_p and eigenfunctions $w_p(\mathbf{r}, \omega)$ define the *fluctuation potentials*.^{5,9} Close to ω_p , $\lambda_p(\omega)$ varies

linearly,

$$\lambda_p(\omega) \approx \lambda'_p(\omega - \omega_p) + i\Gamma_p, \quad (24)$$

where $\lambda'_p = d[\text{Re } \lambda_p(\omega)]/d\omega|_{\omega_p}$. This approximation yields a Lorentzian behavior for the quasi-bosonic peaks in $\beta(\omega)$ of width $\gamma_p = \Gamma_p/\lambda'_p$, which also limits the range of the density fluctuations and the screened potential $w_p(\mathbf{r}, \omega_p)$. Nevertheless, we have found that an explicit matrix inversion on a finite real-space basis (see below) usually converges well for all frequencies due to the finite imaginary part of the dielectric screening $\epsilon(\omega)$.

Formally, the Lindhard expression for the independent particle response function on the real-axis can be expressed in terms of the one-particle Green's function²⁷

$$\chi^0(\mathbf{r}, \mathbf{r}', \omega) = 2 \int_{-\infty}^{E_F} dE [\rho(\mathbf{r}, \mathbf{r}', E) G(\mathbf{r}', \mathbf{r}, E + \omega) + \rho(\mathbf{r}', \mathbf{r}, E) G^*(\mathbf{r}, \mathbf{r}', E - \omega)], \quad (25)$$

$$\frac{-1}{\pi} \text{Im } \chi^0(\mathbf{r}, \mathbf{r}', \omega) = 2 \int_{E_F - \omega}^{E_F} dE \rho(\mathbf{r}, \mathbf{r}', E) \rho(\mathbf{r}', \mathbf{r}, E + \omega). \quad (26)$$

Here $\rho(\mathbf{r}', \mathbf{r}, E)$ is the spectral density of the one-particle Green's function which under the integrals can be replaced with $(-1/\pi) \text{Im } G(\mathbf{r}', \mathbf{r}, E)$ (cf. Eq. (33) and (34) of Ref 28). The convolution in $\text{Im } \chi^0(\omega)$ defines a particle-hole spectral function. The calculation of $W_c(\mathbf{r}, \omega)$ thus requires both Re and $\text{Im } \chi^0(\mathbf{r}, \mathbf{r}', \omega)$, and hence expressions for both $\rho(\mathbf{r}, \mathbf{r}', E)$ and $G(\mathbf{r}, \mathbf{r}', \omega)$. Explicit derivations and algorithms for these functions are given in Ref. 27, along with algorithms for calculating XAS and optical response, based on summations over a finite cluster surrounding the absorbing atom. Below, we show how $\chi^0(\mathbf{r}, \mathbf{r}', \omega)$ and $\chi(\mathbf{r}, \mathbf{r}', \omega)$ can be calculated within a generalized real-space multiple-scattering Green's function (RSGF) approach using a discrete site-radial coordinate basis.

D. Real-Space Multiple Scattering Formalism

The key ingredients in the RSGF calculation of $W_c(\mathbf{r}, \omega)$ are the bare response function $\chi^0(\mathbf{r}, \mathbf{r}', \omega)$ which is defined in Eq. (23) in terms of the independent particle Green's functions $G(\mathbf{r}, \mathbf{r}', E)$, and the interaction kernel $K = v + f_{xc}$ which here is approximated by the RPA $K = v$. The most demanding step is the inversion of the non-local dielectric matrix $\epsilon(\mathbf{r}, \mathbf{r}', \omega)$ on a 3- d grid, which can be computationally formidable. In order to simplify the calculation, we employ a generalization of real-space multiple-scattering (RSMS) formalism with a discrete site-radial coordinate basis, analogous to that developed for x-ray spectra and optical response.^{1,27} In this approach, space is partitioned into cells i with cell boundaries defined by $\Theta_i(\mathbf{r}) = 1$ (0) for points inside (outside) a given cell. Formally the cell boundaries should be defined by Voronoi or equivalent partitioning.

However, for simplicity, the cells are taken to be Norman spheres (i.e., spheres of charge neutrality).^{27,31} Thus $\Theta_i(\mathbf{r}) = \theta(r_N - r_i)$, where $\theta(r)$ is the unit step function, and r_N denotes the Norman radius. The points within each cell are then represented in spherical polar coordinates $\mathbf{r}_i = (r_i, \Omega_i)$. In addition the radial coordinates are typically defined on a discretized logarithmic grid, e.g., $r_{i,n} = \exp(-x_0 + n\delta x)$, as in SCF atomic calculations,³² while the angular dependence is represented by spherical harmonics $Y_{L_i}(\hat{r}_i)$, where $L_i = (l_i, m_i)$. Thus the spatial points \mathbf{r} are represented by the discrete indices $I = (i, n_i, L_i)$, which have a finite volume $\Delta_i = 4\pi r_i^2 \delta_i$, with $\delta_i \approx r_i \delta x$ being the radial grid spacing (e.g., $x_0 = -8.8$ and $\delta x = 0.05$). This construction conserves charge and simplifies volume integration, i.e., for a given volume $\int d^3r = \sum_i \int^{r_N} r_i^2 dr_i d\Omega_i$. With this representation, functions of coordinates $F(\mathbf{r}) \rightarrow F_I$ are represented by vectors, and $F(\mathbf{r}, \mathbf{r}') \rightarrow F_{I,J}$ by matrices in I and J of rank $N_r N_i (l_{max} + 1)^2$, where l_{max} denotes the maximum angular momentum used in the calculation.

This construction is then implemented within the standard RSMS theory, which assumes spherical symmetry of the scattering potentials within each cell. The independent particle Green's functions are given by,¹

$$\begin{aligned} G(\mathbf{r}, \mathbf{r}', E) &= -2k \sum_{iLjL'} [\delta_{ij} \delta_{LL'} R_{iL}(\mathbf{r}_{i < \mathbf{r}_{i >}) + \\ &\quad R_{iL}(\mathbf{r}_i) \tilde{G}_{iLjL'}(E) R_{jL'}(\mathbf{r}'_j)] \Theta_i(\mathbf{r}) \Theta_j(\mathbf{r}') \\ &= \sum_{iLjL'} [G_{iL}^c(\mathbf{r}_i, \mathbf{r}'_j, E) \delta_{ij} \delta_{LL'} + \\ &\quad G_{iLjL'}^{sc}(\mathbf{r}_i, \mathbf{r}'_j, E)] \Theta_i(\mathbf{r}) \Theta_j(\mathbf{r}'). \end{aligned} \quad (27)$$

Here $R_{iL}(\mathbf{r}) = i^l (R_{il}(r)/r) Y_L(\hat{\mathbf{r}})$ and $H_{iL}(\mathbf{r}) = i^l (H_l(r)/r) Y_L(\hat{\mathbf{r}})$ are the regular and irregular solutions to the single site Dirac equation for the atom at site i , $\mathbf{r}_i = \mathbf{r} - \mathbf{R}_i$ is the position relative to the center of the i^{th} cell, and $\tilde{G}_{iLjL'}(E)$ is the multiple scattering matrix.²⁷ The radial wave-functions $R_L(\mathbf{r}, E) = i^l (R_l(r)/r) Y_L(\hat{\mathbf{r}})$ are scattering-state normalized such that $R_l(r) \rightarrow \sin(kr - l\pi/2 + \delta_l)$ beyond the muffin-tin radius r_{mt} ,³³ where δ_l are partial wave phase shifts and $k = \sqrt{2E}$ is the photoelectron momentum. Thus,

$$G(\mathbf{r}, \mathbf{r}', E) = \sum_{iLjL'} Y_L^*(\hat{r}_i) G_{iLjL'}(r_i, r'_j) Y_{L'}(\hat{r}'_j), \quad (28)$$

where the cell functions Θ_i and Θ_j have been absorbed into the definition of $G_{iLjL'}(r_i, r'_j, E)$. On the real axis, the density matrix $\rho = \text{Im} G$ can be expressed similarly,

$$\begin{aligned} \rho(\mathbf{r}, \mathbf{r}') &= \sum_{iLjL'} R_{iL}(\mathbf{r}_i) \tilde{\rho}_{iLjL'}(E) R_{jL'}(\mathbf{r}'_j) \Theta_i(\mathbf{r}) \Theta_j(\mathbf{r}'), \\ &= \sum_{iLjL'} Y_L(\hat{r}_i) \rho_{iLjL'}(r_i, r'_j, E) Y_{L'}(\hat{r}'_j). \end{aligned} \quad (29)$$

Additional details of the method and algorithms for calculations of the quantities involved in Eq. (27) can be

found elsewhere.^{1,27} With the above representation of the Green's function and density matrix, the bare response function $\chi^0(\omega)$ can be expressed similarly in a site, radial-coordinate, and angular momentum basis,

$$\chi^0(\mathbf{r}, \mathbf{r}', \omega) = \sum_{iLjL'} Y_L(\hat{r}_i) \chi_{iLjL'}^0(r_i, r'_j, \omega) Y_{L'}(\hat{r}'_j). \quad (30)$$

Likewise, we expand the interaction kernel K in spherical harmonics about each cell center, and for simplicity given the near spherical symmetry of the core-hole, keep only the spherical terms $L = L' = 0$. If we ignore the TDDFT contribution $f_{xc} = \partial V_{xc}(\rho)/\partial \rho$, as in the RPA, the kernel becomes

$$\begin{aligned} K(\mathbf{r}, \mathbf{r}') &\approx \sum_{ij} Y_{00}(\hat{r}_i) K_{i0j0}(r_i, r'_j) Y_{00}(\hat{r}'_j) \Theta_i(\mathbf{r}) \Theta_j(\mathbf{r}'), \\ K_{i0j0}(r_i, r'_j) &= \left[\frac{4\pi}{r_{i>}^2} \delta_{ij} + \frac{4\pi}{R_{ij}} (1 - \delta_{ij}) \right], \end{aligned} \quad (31)$$

where $R_{ij} = 1/|\mathbf{R}_i - \mathbf{R}_j|$, and $r_{i>} = \max(r_i, r'_i)$.

As a further simplification, we assume here that the deep core-hole density and potential, and hence the screened core-hole potential are spherically symmetric about the central site,

$$\begin{aligned} \rho_c(\mathbf{r}) &= \rho_{c0}(r) Y_{00}(\hat{\mathbf{r}}), \\ V_c(\mathbf{r}) &= V_{c0}(r) Y_{00}(\hat{\mathbf{r}}), \\ W_c(\mathbf{r}, \omega) &= w_c(r, \omega) Y_{00}(\hat{\mathbf{r}}). \end{aligned} \quad (32)$$

Then $W_c(\mathbf{r}, \omega)$ as well as $\beta(\omega)$ depend only on the spherical $L = L' = 0$ components of the bare response function. The matrix inversion of $\epsilon = \mathbf{1} - \mathbf{K}\chi_0$ can then be expressed in terms of a matrix inverse in the site and radial coordinates

$$\chi = \chi^0 [\mathbf{1} - \mathbf{K}\chi^0]^{-1}. \quad (33)$$

From Eq. (24), the matrix elements χ_{IJ}^0 in the discrete basis $I = (i, r_i)$ and $J = (j, r'_j)$ are

$$\begin{aligned} \chi_{I,J}^0(\omega) &= \frac{1}{2\pi} \int_{-\infty}^{E_F} \sum_{LL'} \Delta_i^{1/2} \Delta_j^{1/2} \rho_{iLjL'}(r_i, r'_j, E) \times \\ &\quad [G_{jL'iL}(r'_j, r_i, E + \omega) + G_{jL'iL}^*(r'_j, r_i, E - \omega)]. \end{aligned} \quad (34)$$

Examining the above equations and Eq. (27), we see that site off-diagonal terms $i \neq j$ contribute to the full response function in several ways: i) off-diagonal terms in χ^0 corresponding to the free propagation of a particle-hole from one site to another; ii) off-diagonal terms in the interaction kernel K , corresponding to the coupling of a particle-hole state at site i with another at site j ; iii) a combination of these two, corresponding to the propagation of a particle-hole state from one site to an intermediate site, then scattering into another particle-hole state at a third site; and iv) the Green's function itself has contributions due to scattering of the single particle (photoelectron or valence hole) from neighboring sites.

To summarize, the expressions for $\beta(\omega)$ in the discrete site-radial coordinate basis are

$$\begin{aligned}\beta(\omega) &= \text{Im}[\rho_{c0}\mathbf{W}_{c0}]\theta(\omega), \\ &= \text{Im}[\mathbf{V}_{c0}\chi\mathbf{V}_{c0}]\theta(\omega), \\ &= \text{Im}[\mathbf{W}_{c0}^*\chi^0\mathbf{W}_{c0}]\theta(\omega),\end{aligned}\quad (35)$$

where the vectors are given by

$$\begin{aligned}\rho_{c0} &= \rho_{cI}\delta_{i0}, \\ \mathbf{V}_{c0} &= \mathbf{K}\rho_{c0}, \\ \mathbf{W}_{c0} &= (\mathbf{1} - \mathbf{K}\chi^0)^{-1}\mathbf{V}_{c0}.\end{aligned}\quad (36)$$

The last line in Eq. (35) can also be recast in terms of matrix elements of the screened core-hole potential

$$W_{iL}(E, \omega) = \int^{r_N} dr R_{il}(r_i, E) w_c(r, \omega) R_{il}(r_i, E + \omega). \quad (37)$$

This reveals a striking resemblance to the RSMS theory of XAS,¹ or more precisely, that of optical response,²⁷ the difference being that the dipole transition operator $d(r)$ is replaced by the dynamically screened core-hole potential $w_c(r, \omega)$,

$$\begin{aligned}\beta(\omega) &= \int_{E_F}^{E_F+\omega} dE \sum_{iLjL'} W_{iL}^*(E, \omega) \rho_{iLjL'}(E) \times \\ &\quad \rho_{iLjL'}(E + \omega) W_{jL'}(E, \omega).\end{aligned}\quad (38)$$

E. Local RSGF cumulant approximation

The first line in Eq. (35) shows that the screened core-hole potential is only needed locally about the absorbing atom, since it is multiplied by the density of the core-orbital. For example, for the $1s$ state of Na, the required range is only $\sim 1/11$ Bohr. This suggests that it may be possible, at least in some systems, to treat the problem locally, neglecting site off-diagonal terms in K and χ^0 , while in other systems it may be sufficient to approximate the contribution from off diagonal terms. To do this, the Green's functions in χ^0 are taken to be those of an atom embedded in an electron gas at the interstitial density r_s , for points r, r' outside the Norman radius of the absorbing atom, while the full Green's function is used within the Norman radius. Thus outside the absorbing cell, the Green's function is approximated simply in terms of phase-shifted spherical Bessel functions centered about the absorbing site. The dielectric matrix $\epsilon = \mathbf{1} - \mathbf{K}\chi^0$ is then inverted on a single radial grid, which greatly simplifies the calculations. In this case the matrix equations Eq. (33) and (36) still apply, but are limited to $i = 0$, and the radius R_{\max} defining the central cell is treated as a convergence parameter. The equation for $\beta(\omega)$ then becomes

$$\beta(\omega) = \frac{1}{\pi} \int_0^{R_{\max}} dr \rho_c^0(r) w_c^0(r, \omega). \quad (39)$$

If we further assume that the Green's function has the structure of that of a spherical system, i.e., $G_{L,L'} = G_l \delta_{LL'}$, one can express $\beta(\omega)$ in terms of a joint density of states, [cf. Eq. (32) of Prange et al.,²⁷

$$\beta(\omega) = 2 \sum_l (2l+1) \int_{E_F-\omega}^{E_F} dE |W_l(E, \omega)|^2 \rho_l(E) \times \rho_l(E + \omega) \theta(\omega), \quad (40)$$

where $\rho_l(E)$ is the angular-momentum projected density of states (LDOS) for a given l calculated at the central atom, and the factor of 2 accounts for spin degeneracy.

With spherical symmetry of the core-hole density, calculations of $\beta(\omega)$ reduce to a form with only radial coordinates. The spherical part of the independent particle response function $\chi^0(r, r', \omega)|_{l=0}$,²⁷ is

$$\begin{aligned}\chi_{l=0}^0(r, r', \omega) &= \frac{1}{2\pi} \int_{-\infty}^{E_F} dE \sum_l (2l+1) \rho_l(r, r', E) \times \\ &\quad \times [G_l(r, r', E + \omega) + G_l^*(r, r', E - \omega)].\end{aligned}\quad (41)$$

Here we have used the symmetry and reality of $\rho_l(r, r', E)$ and $G_l(r, r', E)$. In order to stabilize this expression, we split the two terms of the energy integral as follows

$$\begin{aligned}\chi_{l=0}^0(r, r', \omega) &= \frac{1}{2\pi} \sum_l (2l+1) [\chi_l^0(I) + \chi_l^0(II)], \\ \chi_l^0(I) &= \int_{E_F-\omega}^{E_F} dE \rho_l(r, r', E) G_l(r, r', E + \omega), \\ \chi_l^0(II) &= -\frac{1}{\pi} \text{Im} \int_{E_F}^{E_F+\omega} dE G_l(r, r', E) G_l(r, r', E - \omega).\end{aligned}\quad (42)$$

The second of the above integrals can be performed in the complex energy plane where the Green's function is smoother. Note also that these expressions implicitly include fine-structure in $G_l(r, r', \omega)$ from multiple-scattering from atoms beyond the central atom. Finally the screened core hole potential $w_c(r, \omega)$ is defined by a the radial integral,

$$w_c(r, \omega) = \int dr' [1 - K\chi^0(\omega)]_{l=0}^{-1}(r, r') v_c(r'), \quad (43)$$

which can be calculated directly by matrix inversion in the radial coordinate basis for the single site $i = 0$. We use this local RSGF approximation in all of our results shown below.

Eq. (40) is also consistent with the Anderson edge-singularity exponent α for XAS. For metallic systems, $\beta(\omega) \approx \alpha \omega$ is roughly linear in frequency for small ω , reflecting the behavior of the joint density of states near the Fermi energy. The coefficient α can be determined from the zero frequency limit, with matrix elements given by their values at the Fermi level. Since the screened core-hole potential is well localized and spherically symmetric near $\omega = 0$,

$$\alpha = 2 \sum_l (2l+1) |W_l(E_F, \omega = 0)|^2 \rho_l(E_F)^2. \quad (44)$$

This result is consistent with that derived by Anderson, Nozieres and De Dominicis³⁴ $\alpha = 2\sum_l(2l+1)(\delta_l/\pi)^2$. This can be verified by noting that $\rho_l(E) = dN_l/dE$, and $W_l(E_F) = \Delta E_l$ is the change in energy of levels l due to the screened core-hole potential $W(r, 0)$, so $W_l(E_F)\rho_l(E_F) = \Delta N_l = \delta_l/\pi$, i.e., the screening charge in level l , as in the Friedel sum rule. This singular behavior shows up as an asymmetry in the main peak of the XPS. The XAS has an additional contribution from the Mahan edge singularity exponent $\alpha_l = -2\delta_l/\pi$, where the photoelectron has local angular momentum l .³⁵ Even in insulators, the low energy background terms tend to grow linearly beyond the gap, leading to an asymmetry in the quasi-particle peak, though without a true singularity.

III. DETAILS OF THE CALCULATIONS

The RSGF formalism used here has been implemented within the FEFF10 code,¹⁹ with the RPA approximation for the TDDFT kernel $K = 1/|\mathbf{r} - \mathbf{r}'|$. The one-particle Green's functions are calculated using self-consistent-field (SCF) potentials, full-multiple-scattering,^{1,24} and unless noted otherwise, the final-state-rule approximation with a screened core hole in the final state. The RSGF calculations of $w_c(r, \omega)$ depend on the radius R_{max} beyond which the response functions are truncated, the maximum angular momentum l_{max} , the radius r_{fms} of the cluster of atoms used in the full-multiple-scattering calculations, and a small imaginary part γ added to the energy of the Green's functions; the value of γ is set to 0.1 eV for all calculations except for the electron gas where it is set to 0.01 eV. R_{max} is treated as a convergence parameter for metallic systems and set to the Norman radius for insulators. By default, we use a dense logarithmic grid e.g., $r_{i,n} = \exp(-8.8 + 0.05n)$, as in the Dirac-Fock atomic calculations in FEFF10.³² Typically this amounts to about 200 points per cell for each frequency, which is computationally manageable, though a sparser grid may be adequate in some cases. For the calculations of the cumulant spectral function, broadening by a Voigt function with both Gaussian and Lorentzian half-widths of 0.25 eV is used for all systems. Finally, for calculations of the 2p XPS, several additional parameters were used. First, a parameter is introduced to account for the spin-orbit splitting between the $2p_{1/2}$ and $2p_{3/2}$ contributions; second, a Gaussian broadening with width Γ_{exp} was applied to the spectrum to account for experimental broadening, and separate Lorentzian widths $\Gamma_{2p_{1/2}}$ and $\Gamma_{2p_{3/2}}$ to account the different for core-hole lifetimes; third, a Shirley background³⁶ was calculated from, and then added to the theoretical spectrum with a scaling parameter B to match the low energy limit of the experimental data. Below we present results only for the local RSGF spherical approximation, which is found to be semi-quantitative in comparison to experiment for the systems treated here. A more complete treatment including longer-ranged contributions with the generalized

RSMS formalism is reserved for the future.

IV. RESULTS

A. Homogeneous electron gas

As a first illustration and proof of principle, we present results for the homogeneous electron gas (HEG). An approximate treatment of the cumulant for this system was described by Langreth,³ and in more detail by Lundqvist and Hedin^{5,37} for the plasmon-pole (PP) and RPA approximations. For a deep core-level, the core charge density can be approximated by a point charge, so that the excitation spectrum $\beta(\omega)$ is given by a one-dimensional integral in momentum space,

$$\beta(\omega) = \frac{2}{\pi^2} \int dq \text{Im} [\epsilon^{-1}(q, \omega)] \theta(\omega). \quad (45)$$

This can be computed numerically within the RPA, or analytically with the plasmon pole model.³⁸ The results are shown in Fig. 1, where $\beta(\omega)/\omega$ calculated with RSGF at several truncation radii r_{max} are compared to the numerically exact q -space results and with the single plasmon-pole model.³⁷ Consistent with the q -space formulation, the behavior of $\beta(\omega)$ exhibits a linear part at low energy due to the particle-hole continuum, where $-\text{Im} \epsilon(\mathbf{q}, \omega)^{-1} \approx \text{Im} \epsilon(q, \omega)/|\epsilon(q, 0)|^2$ and $\epsilon(q, 0)$ is finite, as well as a sharply peaked structure above the plasmon onset $\omega_p \approx 6.0$ eV corresponding to the zeros of $\epsilon(q, \omega)$. The adiabatic approximation is also shown, which compares well at low frequencies. Note that the RSGF for-

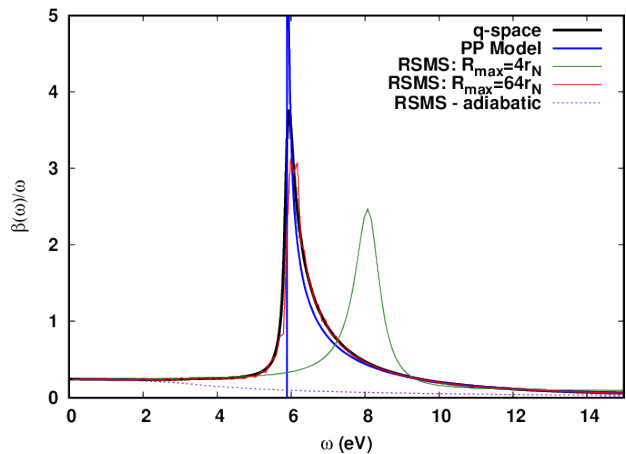


FIG. 1: Cumulant kernel $\beta(\omega)/\omega$ for the HEG at $r_s = 4$ calculated using the RSGF approach compared to that based on the q -space formula in Eq. (45) and the plasmon-pole model.^{5,37} RSMS calculations are shown for $R_{max} = 4r_N$ and $R_{max} = 64r_N$, where the Norman radius $r_N = 1.4 \text{ \AA}$ was chosen as that for bcc sodium. Note that the low frequency, nearly constant behavior of $\beta(\omega)/\omega$, gives the edge singularity index α . The dashed purple curve shows the adiabatic result which gives a good approximation for α .

mulation (red) performs well at all energies except near the plasmon peak, where it loses some spectral weight. This is likely due to the truncations of $R_{max} = 64r_N$ and $l_{max} = 25$. The calculations also agree well with the PP model⁵ above the plasmon frequency ~ 6 (eV); however the PP approximation completely ignores the low energy contribution.³⁸ This low frequency tail in the HEG is dominated by the particle-hole contribution to the dielectric function and is linear in ω . This behavior accounts for the Anderson edge singularity in x-ray spectra and an asymmetric quasi-particle line-shape in XPS $J_k(\omega) \sim \omega^{\alpha-1}$. For the HEG for $r_s = 4$, we obtain $\alpha = 0.24$, which compares well to the experimental value 0.21 ± 0.015 for the 1s XPS of sodium, a nearly free electron system with $r_s \approx 4$.³⁹ We also analyzed the extent to which the calculation of $\beta(\omega)$ can be approximated locally. The green curve in Fig. 1 shows the result from RSGF calculations with $R_{max} = 4r_N$ in the radial arguments of $\chi^0(r, r', \omega)$. While the linear portion is reproduced very well, the position of the plasmon peak is overestimated by ~ 2 (eV) or 30%. Although difficult to see, the high energy tail is poorly represented and only corrected with much larger $r_{max} = 64r_N$. The RSGF spectrum approaches the q -space result with increasing R_{max} , but does not converge until $R_{max} = 64r_N \sim 177$ Bohr. This difference in convergence in different energy ranges reflects the fact that the sharp peak in $\beta(\omega)$ is largely defined by the sharp plasmon peak in the loss function, which is dominated by momentum transfer q near zero. On the other hand, the linear behavior near $\omega = 0$ and the long tail at high frequency are due to the particle-hole continuum and the dispersion of the plasmon respectively. These depend on higher values of momentum transfer which results in faster convergence with R_{max} . Fig. 2 shows the screened core-hole potential $w_c(r, \omega)$ (also for $r_s = 4$) scaled for convenience by the bare potential $V_c(r)$ vs r for frequencies from 0 eV to well above the ω_p . The RSGF result (solid) are compared with the results of the plasmon pole (dot dashes) and those from the RSRT formulation (dashes). As expected physically, there is little screening at small $r \ll r_s$ for all frequencies due to the slow build-up of the induced density response. For $r > r_s$ the zero frequency curve (red) exhibits extremely efficient Yukawa-like screening, while the behavior at high frequencies is weakly screened, with $w_c(r, \omega)$ remaining finite at large r . Near the plasma-frequency $\omega_p \approx 6$ eV $w_c(r, \omega)$ oscillates sinusoidally, corresponding to delocalized charge density fluctuations with substantial contributions to $\text{Im} w(r, \omega)$. The oscillatory behavior matches reasonably well with that of the plasmon pole model, although there is more damping and larger screening in the high frequency curves calculated with RSGF, and the oscillations are slightly phase shifted. Some of these differences are expected due to differences in the plasmon dispersion and the lack of particle-hole continuum states in the plasmon pole model. The majority of the damping seen in the RSGF results comes from the truncation of

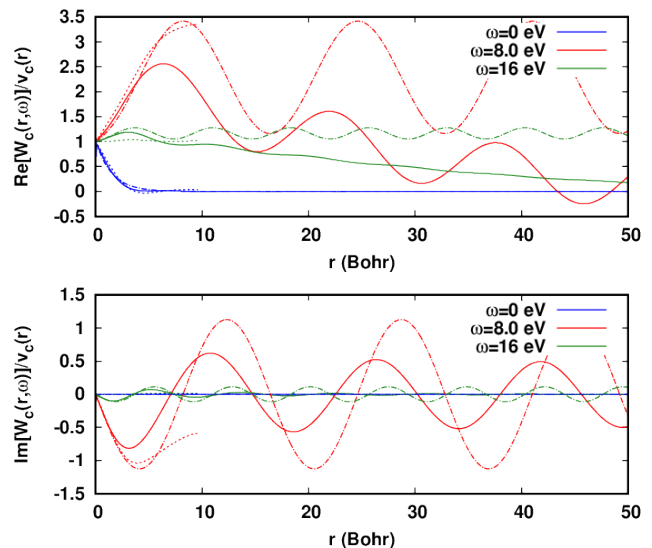


FIG. 2: Screened core-hole potential from the RSGF approach (solid) relative to the bare core potential $\text{Re} w_c(r, \omega)/V_c(r)$ (top) and $\text{Im} w_c(r, \omega)/V_c(r)$ vs r for the HEG at $r_s = 4$ for $\omega = 0$, $\omega = 8$ eV $\approx \omega_p$, and $\omega = 16$ eV $\gg \omega_p$. Note that the behavior becomes strongly delocalized, oscillatory, and lossy near ω_p . For comparison results from the RSRT approach (dashes) and the plasmon pole model (dot dashes) are also shown.

the real-space grid, although this damping does not affect the calculated values close to the origin, which determine $\beta(\omega)$.

B. Nearly free-electron system

As an example of the RSGF approach that can be compared with the HEG, we present calculations for bcc Na, a nearly free electron (NFE) system with $r_s \approx 4$. This is illustrated in Fig. 3 for a range of r_{fms} and for large R_{max} . The behavior of $\beta(\omega)$ is clearly linear below ω_p and comparable to that of the HEG at high energies as well. Moreover, the behavior near the plasmon peak also has long range oscillatory contributions. For such NFE systems, scattering from near-neighbor neighbors appears to be less important than a large R_{max} alone, as the results converge reasonably well by setting $r_{fms} = 0$. The oscillatory behavior near the peak reflects the discrete nature of plasmon excitations within a sphere of finite R_{max} .

C. Transition metal compounds

Next we consider several early transition metal compounds, which are typically moderately correlated. We first present results for TiO_2 (rutile), which was previously studied with the RSRT approach.¹⁶ The strong peak in $\beta(\omega)$ for TiO_2 is shown in Figs. 3 (bottom) and 4 (top). Unlike the behavior of Na, the spectrum is largely

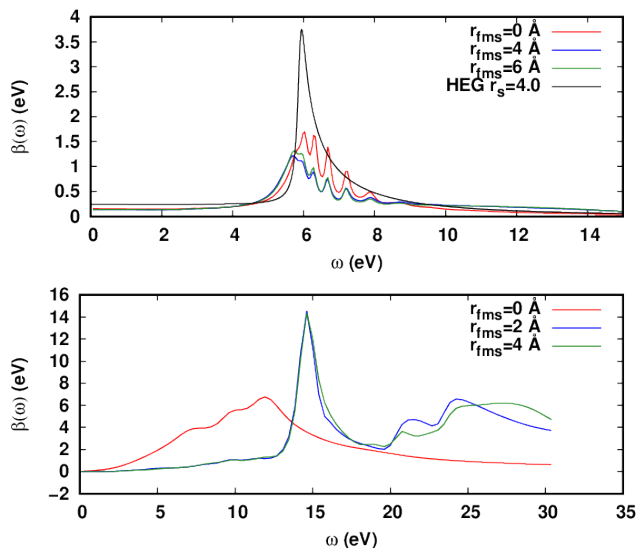


FIG. 3: RSGF calculation of the cumulant kernel $\beta(\omega)$ for Na (top) and TiO_2 (bottom), with varying FMS cluster size r_{fms} . Note that scattering from the nearest-neighbor atoms has a drastic effect in TiO_2 but is much smaller for Na. Both spectra show minimal differences with the inclusion of atoms beyond the nearest-neighbors.

independent of R_{max} , while r_{fms} has a drastic effect on the position and intensity of the main peak in $\beta(\omega)$ as seen in Fig. 3. The independence of the spectrum with respect to R_{max} suggests a localized nature of the excitations in TiO_2 . The main peak is neither directly related to peaks in $\chi^0(\omega)$ nor in $\text{Im } \epsilon(\omega)$. Instead the peak is consistent with zero-crossings of $\text{Re } \epsilon(\omega)$. For TiO_2 we have found that there is a single dominant eigenvalue of the dielectric matrix at ω_p , although the lack of more than one crossing may be due to the limited spatial extent of our calculations. Consequently a fluctuation potential treatment [cf. Eq. (22) and (23)] is appropriate. This PP model yields a Lorentzian shape for $\beta(\omega)$ and $\text{Im } w_c(r, \omega)$, as seen in Fig. 4 (top, green) as well as a finite range of $w_c(r, \omega)$ varying inversely with γ_p . The cumulant kernel $\beta(\omega)$ calculated with Eq. (40) and $R_{max} = r_N$ is shown in Fig. 4 (top), along with a comparison to the RSRT method.

In contrast to the HEG, the adiabatic approximation (top, purple) does not reflect the spectrum of $\beta(\omega)$, even at low frequencies, and is in error by $\sim 50\%$ by ≈ 2.5 eV, which is about where the first excitation feature occurs. Instead, almost all structure in $\beta(\omega)$, or at least that above ≈ 7 eV, reflects that of $|W_c(\omega)|^2$. Below 7 eV, the spectrum has little structure. The prominent peak at about 15 eV stems from the single pole of $\epsilon^{-1}(\omega)$ where $\lambda_p(\omega)$ and hence $\text{Re } \epsilon(\omega)$ crosses zero. The low energy structure is similar for both RSGF and RSRT methods, and the agreement of the peak near 15 eV is semi-quantitative. Finally, at higher energies there is appreciable difference between the RSGF and RSRT results, which could be due to the limited basis set and lack of

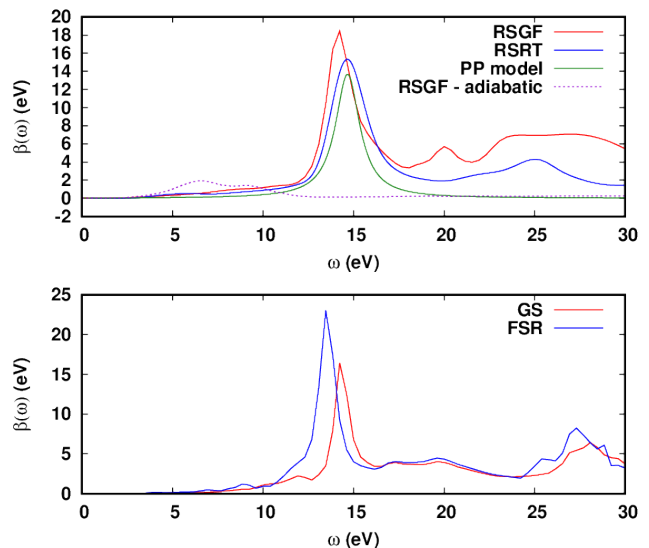


FIG. 4: Cumulant kernel $\beta(\omega)$ for TiO_2 (Top) calculated with the RSGF approach (red), and for comparison the RSRT (blue), the fluctuation potential approach with a single pole (PP), and the adiabatic limit (dashed). The lower figure for ScF_3 (Bottom) compares results calculated with ground state electronic structure (GS), and with the final state rule (FSR). The core-hole shifts the peak to lower energy by ~ 0.8 eV, in better agreement with experiment.

continuum states in the RSRT results, which rely on local basis functions, or the local approximation of the RSGF method. Note however, that the structure above 15 eV does not contribute significantly to the spectral function, due to the factor of $1/\omega^2$ in the cumulant $C_c(t)$ in Eq. (4). Results for ScF_3 (bottom) are similar, with a large peak at about 13 to 14 eV depending on whether the calculation was performed with (FSR), or without (GS) a core-hole. The inclusion of the core-hole red-shifts the spectrum, and increases the main peak intensity, similar to the effects seen in x-ray absorption near-edge spectra. This excitonic shift improves the agreement with experiment, which shows a peak at about 12 eV (see Fig. 8). The spectral functions, which are closely related to XPS, are shown in Fig. 5 for Na, TiO_2 and ScF_3 , calculated using Eq. (1). The spectral function of Na is compared with that of the homogeneous electron gas, and is shown for several values of r_{fms} , while that of TiO_2 (middle) is compared to the result from RSRT, and shows good agreement. Finally, the spectral function of ScF_3 is shown as calculated with (FSR) and without (GS) a final-state-rule core-hole. In these curves, we see a large main peak at high energy, corresponding to the quasi-particle peak, and satellite peaks at lower energy, which reflect the behavior of $\beta(\omega)/\omega^2$. The quasi-particle peak in the spectral function of Na shows an appreciable asymmetry, corresponding to the edge singularity, and originating from the linear behavior in $\beta(\omega)$ at low frequency.

The dynamical screening fraction of the core-hole po-

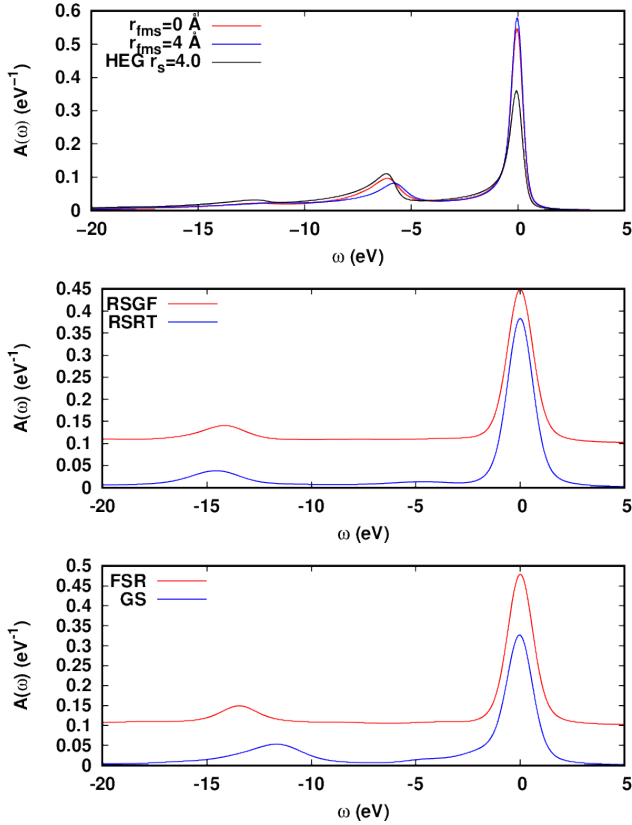


FIG. 5: Spectral functions $A(\omega)$ for Na (Top) compared with the HEG with different r_{fms} . The middle figure compares the RSGF and RSRT¹⁶ approaches for TiO₂, and the bottom figure compares the spectral function of ScF₃ calculated with (FSR) and without (GS) the final state rule core-hole.

tential which here is defined as $f(r, \omega) = [w_c(r, \omega) - V_c(r)]/V_c(r)$, calculated from Eq. (43) with the local RSGF cumulant is shown for Rutile TiO₂ in Fig. 6 for a few selected energies. The bare core-hole potential $V_c(r)$ is that for the $1s$ core-level of Ti and is nearly Coulombic for a point charge, i.e., $V_c(r) \approx 1/r$ beyond the Ti $1s$ radius $r_{1s} \approx 1/22$ Bohr. The screening fraction $f(r, \omega)$ is small near $r = 0$ (i.e., little screening), and fairly strong $f(\omega) \approx -1$ beyond the Thomas-Fermi screening length r_0 . However, near the peak at $\omega_p \approx 14.8$ eV, abrupt changes occur, with the system becoming over-screened ($f(\omega)$ reaching about -2 at 14 eV) or under-screened ($f(\omega) < 0.25$) above 15.4 eV. The imaginary part of W_c largely reflects the structure in $\beta(\omega)$, starting at 0 for $\omega = 0$, and rising to a peak at $\omega_p \approx 14.8$ eV, then rapidly subsiding, although it is still appreciable at high energy. Note that the behavior of $W_c(r, 0)$ is metallic, quickly going to zero beyond the Thomas-Fermi screening radius, which is likely due to both the finite cluster size in the calculation of the Green's functions, which produce only a pseudo-gap in the material, and the neglect of off-diagonal elements in the interaction kernel K and response function χ^0 . However, this unphysical

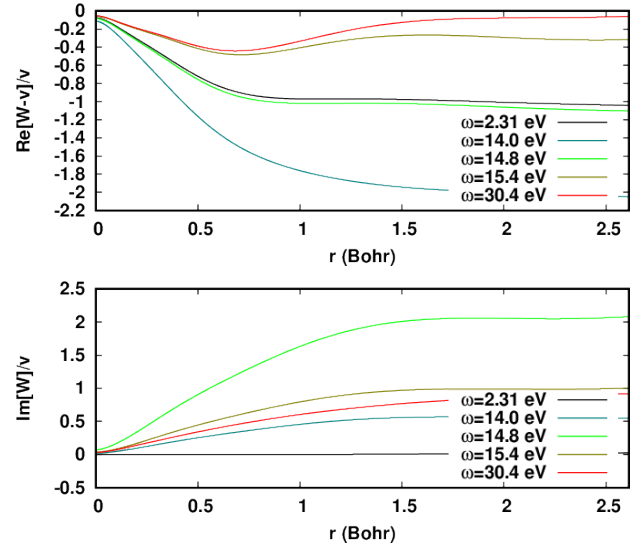


FIG. 6: Screening fraction $f(r, \omega) = [w_c(r, \omega) - V_c(r)]/V_c(r)$ relating the dynamically screened $w_c(r, \omega)$ and bare $V_c(r) \approx 1/r$ core-hole potentials for the Ti core-hole in TiO₂ at a few selected energies. Note that the screening is local and strong at low (black), weak at high (red), and becomes lossy and delocalized near ω_{CT} with roughly a Lorentzian line-shape. The behavior at large r is only semi-quantitative due to the truncation of r_{max} .

behavior does not seem to affect $\beta(\omega)$ appreciably. We also note that the satellites in the TiO₂ spectral function correspond to the ≈ 13 eV peak seen in experimental XPS, which have been interpreted both as charge-transfer excitations,^{16–18,40} as well as plasmons.⁴¹ Although distinction between plasmon vs charge transfer excitations may be a question of semantics,^{42–44} the behavior of the excitation in TiO₂ and the other transition metal compounds is rather different from the plasmons found in FEG-like materials, where the lattice has little effect on the plasmon energy. The apparently localized nature of the excitations in TiO₂ is consistent with the definition of charge transfer excitations. Nevertheless, for the systems investigated here, the excitations at ω_p corresponds to a zero crossing of the dielectric matrix.

Finally, we compare calculated and experimental metal $2p$ XPS of TiO₂, ScF₃, and ScCl₃ in Figs. 7 and 8, which show the spectra as a function of energy relative to the $2p_{3/2}$ main peak. The main $2p_{3/2}$ peak is centered at $E = 0$ eV, and the first peak below that is the $2p_{1/2}$ main peak, seen at ≈ -6 eV in TiO₂, and ≈ -5 eV in the Sc halides. Below the $2p_{1/2}$ peaks, two satellites can be seen, corresponding to a many-body excitation beyond the main $2p_{3/2}$ or $2p_{1/2}$ peak, lowering the photoelectron energy by the energy of the excitation ΔE . Experimentally, the satellite energy is the largest in TiO₂ at $\Delta E \approx 13.4$ eV, followed by ScF₃ with $\Delta E \approx 12.3$, then ScCl₃ at $\Delta E \approx 10$ eV. This trend is reproduced by the calculations, although the satellite energies are slightly overestimated for TiO₂ and ScF₃, and slightly underes-

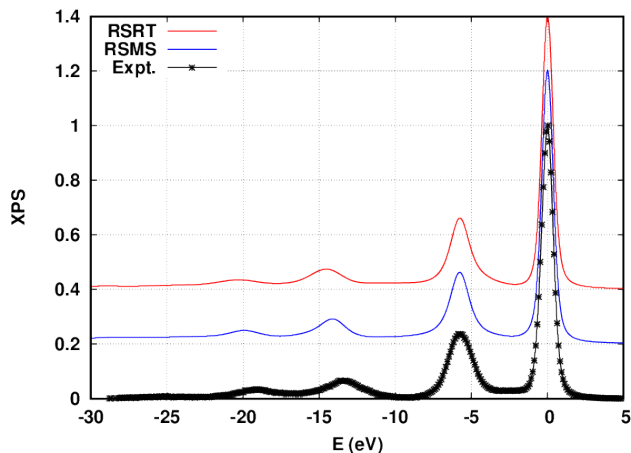


FIG. 7: Comparison of the RSGF Ti 2p spectral function with the RSRT approach and XPS experiment.⁴⁵

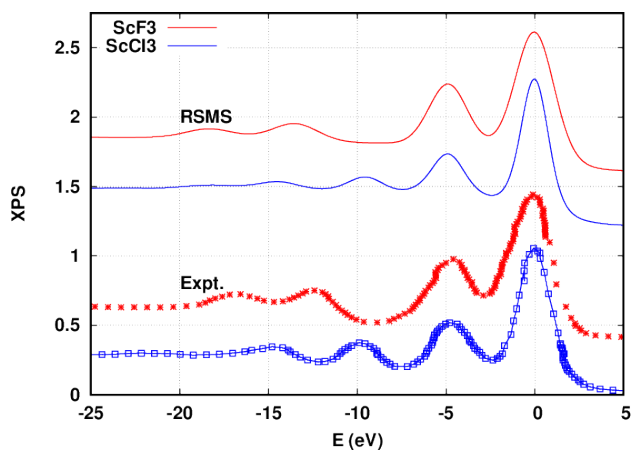


FIG. 8: Comparison of the Sc 2p XPS of ScF_3 (red) and ScCl_3 (blue) calculated with the RSGF approach and with experiment (dots). The experimental data was digitally reproduced from Ref. 45

estimated for ScCl_3 , with $\Delta E \approx 14.1$ eV, 13.4 eV, and 9.5 eV respectively. The intensities of the satellites are also slightly underestimated by the local RSMS theory as well as that of the RSRT (shown for TiO_2). The satellite energies are inversely correlated with the metal ligand bond-length in the material, with the bond-lengths at 1.95 Å for TiO_2 , 2.03 Å for ScF_3 , and 2.51 Å for ScCl_3 . This is reminiscent of XAS, where an expansion of the bond contracts the oscillatory fine-structure in the spectrum. This likely explains the trend between ScF_3 and ScCl_3 , although the differing oxidation state of Ti in TiO_2 may also play a role in the satellite energy. Overall, the agreement between the local RSMS theory and experiment is remarkable given the level of approximations made.

V. SUMMARY AND CONCLUSIONS

We have developed an *ab initio* real-space Green's function approach for calculations of intrinsic inelastic losses in x-ray spectra. These losses show up e.g., as satellites in XPS and reduced fine-structure amplitudes in XAS, but are often neglected in conventional calculations. The approach is based on the cumulant Green's function formalism and a generalization of the Langreth cumulant to inhomogeneous systems analogous to that in the RSRT, TDDFT approach. The formalism of the cumulant kernel $\beta(\omega)$ is analogous to x-ray and optical absorption spectra $\mu(\omega)$, except that the (dipole) transition operator is replaced by the core-hole potential $V_c(\mathbf{r})$, with monopole selection rules. Within the RPA, three equivalent expressions for $\beta(\omega)$ are derived, and the link to the GW self-energy is discussed. A generalized real-space multiple scattering (RSMS) formalism with a discretized site-coordinate basis is introduced to carry out the calculations with standard linear algebra. The computational effort further simplifies with spherical symmetry of the screened core-hole potential and response function. The calculations can then be carried out on a one-dimensional radial grid, similar to that in conventional atomic calculations and the RSGF approach for XAS. Solid-state effects from the extended system are included in terms of RSGF calculations of back scattering contributions from atoms beyond the absorption site. The behavior of both $W_c(\mathbf{r}, \omega)$ and $\beta(\omega)$ reflect the analytic structure of the inverse dielectric matrix and the loss function, where the peaks in $\beta(\omega)$ arise from the zeros of $\text{Re} \epsilon(\omega)$. This behavior is consistent with delocalized quasi-boson excitations, which have been interpreted both as plasmons and charge-transfer excitations. Moreover, the low energy $\omega \rightarrow 0$ limit, $\beta(\omega) \approx a\omega$ in metallic systems, is consistent with the Anderson edge singularity exponent. Our local RSGF cumulant approximation yields results in semi-quantitative agreement with the complementary RSRT approach, as well as with experimental XPS, which validates the local approximations. The discrepancy between RSGF and RSRT results is likely due to the neglect of the long range behavior in the bare response function and in the interaction kernel. This behavior is often not well captured by the truncation of the real-space calculations to small R_{max} . Although this is one of the main limitations of the local model, corrections can be added using the more general RSMS formalism with a larger site-radial coordinate basis. Nevertheless, in transition metal oxides like TiO_2 , ScF_3 , and ScCl_3 , the convergence is found to be fairly rapid, yielding reasonable accuracy compared with the RSRT approach. In conclusion, the RSGF approach illustrates the nature and localization of the dynamically screened core-hole $W_c(r, \omega)$ and the cumulant kernel $\beta(\omega)$. The approach permits *ab initio* treatments of the spectral function $A_c(\omega)$ and the quasi-particle XAS $\mu_1(\omega)$ in the convolution in Eq. (2), which can be calculated in parallel with the same RSGF formalism. The approach thereby permits a unified treatment

of XPS and XAS that builds in intrinsic losses. The method can also be applied *ex post facto* to include intrinsic losses in other calculations of x-ray spectra. Many extensions are possible. For example, corrections to the dielectric matrix from next neighbors may be desirable to improve convergence with respect to R_{max} .^{26,27} Although we focused on result within the RPA, generalization to a real TDDFT interaction kernel f_{xc} poses no formal or numerical difficulties. Our generalized RSMS formulation opens the possibility of RSMS approaches to optical spectra beyond the RPA, e.g., within the TDDFT or the Bethe-Salpeter equation formalism. Finally, contri-

butions from extrinsic losses and interference terms can be relevant.^{6,16,46} Further developments along these lines are reserved for the future.

Acknowledgments – We thank T. Fujikawa, L. Reining, E. Shirley and J. Woicik for comments, and S. Adkins and S. Thompson for encouragement. This work is supported by the Theory Institute for Materials and Energy Spectroscopies (TIMES) at SLAC, which is funded by the U.S. DOE, Office of Basic Energy Sciences, Division of Materials Sciences and Engineering, under contract DE AC02-76SF0051.

* jjr@uw.edu

- ¹ J. J. Rehr and R. C. Albers, Phys. Rev. B **41**, 8139 (1990).
- ² J. S. Zhou, L. Reining, A. Nicolaou, A. Bendouan, K. Ruotsalainen, M. Vanzini, J. Kas, J. Rehr, M. Muntwiler, V. N. Strocov, et al., Proc. Nat. Acad. Sci. **117**, 28596 (2020).
- ³ D. Langreth, Phys. Rev. B **1**, 471 (1970).
- ⁴ W. Bardyszewski and L. Hedin, Physica Scripta **32**, 439 (1985).
- ⁵ L. Hedin, Journal of Physics: Condensed Matter **11**, R489 (1999).
- ⁶ L. Campbell, L. Hedin, J. J. Rehr, and W. Bardyszewski, Phys. Rev. B **65**, 064107 (2002).
- ⁷ T. Fujikawa, J. Synchrotron Rad. **8**, 76 (2001).
- ⁸ J. D. Lee, O. Gunnarsson, and L. Hedin, Phys. Rev. B **60**, 8034 (1999).
- ⁹ L. Hedin, J. Michiels, and J. Inglesfield, Phys. Rev. B **58**, 15565 (1998).
- ¹⁰ E. Klevak, J. J. Kas, and J. J. Rehr, Phys. Rev. B **89**, 085123 (2014).
- ¹¹ M. Combescot and P. Nozieres, J. de Physique **32**, 913 (1971).
- ¹² M. Tzavala, J. J. Kas, L. Reining, and J. J. Rehr, Phys. Rev. Research **2**, 033147 (2020).
- ¹³ Y. Liang, J. Vinson, S. Pemmaraju, W. S. Drisdell, E. L. Shirley, and D. Prendergast, Phys. Rev. Lett. **118**, 096402 (2017).
- ¹⁴ S. Biermann and A. van Roekeghem, J. Electron Spectrosc. Relat. Phen. **208**, 17 (2016).
- ¹⁵ P. S. Bagus, C. J. Nelin, C. Brundle, B. V. Crist, N. Lahiri, and K. M. Rosso, Phys. Chem. Chem. Phys. **24**, 4562 (2022).
- ¹⁶ J. J. Kas, F. D. Vila, J. J. Rehr, and S. A. Chambers, Phys. Rev. B **91**, 121112 (2015).
- ¹⁷ J. Woicik, C. Weiland, C. Jaye, D. Fischer, A. Rumaiz, E. Shirley, J. Kas, and J. Rehr, Phys. Rev. B **101**, 245119 (2020).
- ¹⁸ J. C. Woicik, C. Weiland, A. K. Rumaiz, M. T. Brumbach, J. M. Ablett, E. L. Shirley, J. J. Kas, and J. J. Rehr, Phys. Rev. B **101**, 245105 (2020).
- ¹⁹ J. Kas, F. Vila, and J. Rehr (2020).
- ²⁰ F. Aryasetiawan, L. Hedin, and K. Karlsson, Phys. Rev. Lett. **77**, 2268 (1996).
- ²¹ M. Guzzo, G. Lani, F. Sottile, P. Romaniello, M. Gatti, J. J. Kas, J. J. Rehr, M. G. Silly, F. Sirotti, and L. Reining, Phys. Rev. Lett. **107**, 166401 (2011).
- ²² L. D. Landau, J. Phys. **8**, 201 (1944).
- ²³ K. Yabana and G. F. Bertsch, Phys. Rev. B **54**, 4484 (1996).
- ²⁴ J. Kas, F. Vila, C. Pemmaraju, T. Tan, and J. Rehr, J. Synchrotron Rad. **28** (2021).
- ²⁵ C.-O. Almbladh and L. Hedin, 1b, Hrsg. E. Koch (North Holland, Amsterdam 1983) S pp. 607–904 (1983).
- ²⁶ A. L. Ankudinov, Y. Takimoto, and J. J. Rehr, Phys. Rev. B **71**, 165110 (2005).
- ²⁷ M. P. Prange, J. J. Rehr, G. Rivas, J. J. Kas, and J. W. Lawson, Phys. Rev. B **80**, 155110 (2009).
- ²⁸ A. Zangwill and P. Soven., Phys. Rev. A **21**, 1561 (1980).
- ²⁹ M. J. Stott and E. Zaremba, Phys. Rev. A **21**, 12 (1980).
- ³⁰ E. L. Shirley and R. M. Martin, Phys. Rev. B **47**, 15404 (1993).
- ³¹ J. G. N. Jr., Molecular Physics **31**, 1191 (1976).
- ³² J. P. Desclaux, Comp. Phys. Comm. **9**, 31 (1975).
- ³³ A. L. Ankudinov, Ph.D. thesis, University of Washington (1996).
- ³⁴ P. Nozieres and C. T. De Dominicis, Phys. Rev. **178**, 1097 (1969).
- ³⁵ J. J. Rehr, F. D. Vila, J. J. Kas, N. Y. Hirshberg, K. Kowalski, and B. Peng, J. Chem. Phys. **152**, 174113 (2020).
- ³⁶ D. A. Shirley, Phys. Rev. B **5**, 4709 (1972).
- ³⁷ B. I. Lundqvist, Phys. kondens. Materie **6**, 206 (1967).
- ³⁸ See Supplemental Material at [URL will be inserted by publisher] for derivation of the screened potentials within the plasmon pole model.
- ³⁹ P. H. Citrin, G. K. Wertheim, and Y. Baer, Phys. Rev. B **16**, 4256 (1977).
- ⁴⁰ A. E. Bocquet, T. Mizokawa, K. Morikawa, A. Fujimori, S. R. Barman, K. Maiti, D. D. Sarma, Y. Tokura, and M. Onoda, Phys. Rev. B **53**, 1161 (1996).
- ⁴¹ N. Vast, L. Reining, V. Olevano, P. Schattschneider, and B. Jouffrey, Phys. Rev. Lett. **88**, 037601 (2002).
- ⁴² T. Miyakawa, J. Phys. Soc. Jpn. **24**, 768 (1968).
- ⁴³ P. Županović, A. Bjeliš, and S. Barišić, Z. Phys. B **101**, 397–404 (1997).
- ⁴⁴ J. M. F. Gunn and J. C. Inkson, J. Phys. C: Solid State Phys. **12**, 1049 (1979).
- ⁴⁵ D. K. G. de Boer, C. Haas, and G. A. Sawatzky, Phys. Rev. B **29**, 4401 (1984).
- ⁴⁶ P. Cudazzo and L. Reining, Phys. Rev. Research **2**, 012032 (2020).

VI. SUPPLEMENTARY MATERIAL: PLASMON-POLE MODEL

$$\epsilon^{-1}(q, \omega) = 1 + \frac{\omega_p^2}{(\omega + i\delta)^2 - \omega_q^2}. \quad (46)$$

$$W(q, \omega) = \frac{4\pi}{q^2} \epsilon^{-1}(q, \omega). \quad (47)$$

$$\begin{aligned} W(r, \omega) &= \int \frac{d^3q}{(2\pi)^3} \frac{4\pi}{q^2} \epsilon^{-1}(q, \omega) e^{i\mathbf{q}\cdot\mathbf{r}} \\ &= \frac{2}{\pi} \int_0^\infty dq \epsilon^{-1}(q, \omega) \frac{\sin(qr)}{qr} \end{aligned} \quad (48)$$

Expanding $\sin(qr) = [\exp(iqr) - \exp(-iqr)]/2i$, and noting that ϵ^{-1} is an even function of q gives,

$$W(r, \omega) = \frac{1}{i\pi} \int_{-\infty}^\infty \epsilon^{-1}(q, \omega) \frac{e^{iqr}}{qr} \quad (49)$$

The first term in W coming from the 1 in ϵ^{-1} gives the unscreened Coulomb potential $v(r) = 1/r$. The second term $\tilde{W} = W - v$ is given by,

$$\tilde{W}(r, \omega) = \frac{1}{i\pi} \int_{-\infty}^\infty dq \frac{e^{iqr}}{qr} \frac{\omega_p^2}{(\omega - \omega_q + i\delta)(\omega + \omega_q + i\delta)}. \quad (50)$$

For simplicity, we take the dispersion relation $\omega_q = \omega_p + q^2/2$, which gives an integrand with five poles at $q = 0$, $q = \pm\sqrt{2(\omega - \omega_p + i\delta)}$, and $q = \pm i\sqrt{2(\omega + \omega_p)}$. The appearance of $\exp(iqr)$ in the requires that the contour be closed in the upper half plane, so that only the poles with positive imaginary part, as well as the pole on the real axis contribute. Assuming positive frequency only, we have poles at $q = 0$, $q_1 = \sqrt{2(\omega - \omega_p + i\delta)}$, and $q_2 = i\sqrt{2(\omega + \omega_p)}$. The $q = 0$ pole gives a frequency dependent contribution \tilde{W}_0 proportional to the unscreened Coulomb interaction,

$$\tilde{W}_0(r, \omega) = \frac{1}{r} \frac{\omega_p^2}{(\omega + i\delta)^2 - \omega_p^2}. \quad (51)$$

In the zero frequency limit, this term cancels the $v(r)$ in W , which is necessary if the screened Coulomb interaction is going to fall off faster than $1/r$ at large r . The pole at q_1 gives a contribution \tilde{W}_1 which is real and exponentially decaying for $\omega < \omega_p$, and complex and oscillatory for $\omega > \omega_p$, i.e.,

$$\tilde{W}_1(q, \omega) = -\frac{\omega_p^2}{\omega q_1} \frac{e^{iq_1 r}}{q_1 r}. \quad (52)$$

The above term is also the only term that is complex, so that one can immediately find the quasiboson excitation

spectrum by taking the limit of the imaginary part as $r \rightarrow 0$,

$$\begin{aligned} \beta(\omega) &= -\frac{1}{\pi} \lim_{r \rightarrow 0} \frac{\omega_p^2}{\omega q_1} \frac{\sin(q_1 r)}{q_1 r} \theta(\omega - \omega_p) \\ &= \frac{1}{\pi} \frac{\omega_p^2}{\omega q_1} \theta(\omega - \omega_p), \end{aligned} \quad (53)$$

which matches the result found previously for the same model.⁵ Note that the $q = q_1$ contribution becomes unphysically large at low frequency, and is singular at zero frequency, and this is precisely where the $q = q_2$ term is important. This gives a contribution \tilde{W}_2 ,

$$\tilde{W}_2(r, \omega) = \frac{\omega_p^2}{\omega q_2} \frac{e^{iq_2 r}}{q_2 r} \quad (54)$$

At low frequency $\omega < \omega_p$, q_1 becomes imaginary, so that \tilde{W}_1 and \tilde{W}_2 tend to cancel,

$$\begin{aligned} \tilde{W}_1(r, \omega) + \tilde{W}_2(r, \omega) &= \frac{\omega_p^2}{\omega r} \left[\frac{e^{-\kappa_1 r}}{\kappa_1^2} - \frac{e^{-\kappa_2 r}}{\kappa_2^2} \right], \end{aligned}$$

where $\kappa_1 = \sqrt{2(\omega_p - \omega)}$, and $\kappa_2 = \sqrt{2(\omega_p + \omega)}$, $\kappa_0 = \sqrt{2\omega_p}$, $\delta\kappa = \omega/\kappa_0$. Taking the zero frequency limit of the above gives the zero frequency limit of W , since $v - W_0 = 0$ at zero frequency,

$$\lim_{\omega \rightarrow 0} W(r, \omega) = e^{-\kappa_0 r} \left[\frac{\kappa_0}{2} + \frac{1}{r} \right]. \quad (55)$$

Thus in its entirety, the screened potential is,

$$W(r, \omega) = \frac{1}{r} \left[1 + \frac{\omega_p^2}{(\omega + i\delta)^2 - \omega_p^2} \right] \quad (56)$$

$$- \frac{\omega_p^2}{\omega} \frac{e^{-\kappa_2 r}}{\kappa_2^2 r} - \frac{\omega_p^2}{\omega} \frac{e^{iq_1 r}}{q_1^2 r}. \quad (57)$$

Finally, we can take real and imaginary parts of this function to diagnose its behavior at the plasmon frequency.

$$\begin{aligned} \text{Re}[W(r, \omega)] &= \frac{1}{r} \left\{ 1 + \frac{\omega_p^2}{(\omega + \omega_p)(\omega - \omega_p)} \right. \\ &\quad \left. - \frac{\omega_p^2}{2\omega} \left[\frac{e^{-\kappa_2 r}}{\omega + \omega_p} - \frac{e^{-\kappa_1 r}}{\omega_p - \omega} \theta(\omega_p - \omega) \right. \right. \\ &\quad \left. \left. + \frac{\cos(q_1 r)}{\omega - \omega_p} \theta(\omega - \omega_p) \right] \right\}, \end{aligned} \quad (58)$$

$$\begin{aligned} \text{Im}[W(r, \omega)] &= \frac{\omega_p^2}{r} \left[-\frac{1}{\omega + \omega_p} \delta(\omega - \omega_p) \right. \\ &\quad \left. + \frac{\cos(q_1 r)}{2\omega} \delta(\omega - \omega_p) - \frac{\sin(q_1 r)}{\omega q_1^2} \theta(\omega - \omega_p) \right] \\ &= -\frac{\omega_p^2}{\omega q_1} \frac{\sin(q_1 r)}{q_1 r} \theta(\omega - \omega_p). \end{aligned} \quad (59)$$

Reiterating, $W(r, \omega)$ is real for frequencies less than the plasmon frequency $\omega < \omega_p$. At very low frequencies, the potential falls off exponentially, although a Yukawa term is also present, with a growing Coulombic term as frequency increases. At frequencies above the plasmon frequency, the real part also includes an oscillatory term $\sim \cos(q_1 r)/q_1 r$, and an imaginary part appears, which oscillates as $\sim \sin(q_1 r)/q_1 r$. Near $\omega = \omega_p$ is also interesting to analyze. At the plasmon frequency, the second

term in the real part cancels with the last two terms, giving $\text{Re}W \sim 1/r$ at large r , while the imaginary part is singular, with a behavior $\text{Im}W \sim 1/\sqrt{\omega - \omega_p} \theta(\omega - \omega_p)$. This means that somewhere near the plasmon frequency, the oscillations in W become very large, and at high frequency die down, similar to what is seen in Fig. 2. Finally, in the high frequency limit, all terms except the bare Coulomb potential scale as $\sim 1/\omega^2$, so that we essentially retain the bare Coulomb potential, as expected.